




Characterization of deformation structures in P-22 Cr–Mo steel through electron backscatter diffraction and transmission electron microscopy

Dhriti Bhattacharyya^{1,3,*} , Michael Drew^{1,4}, S. R. Humphries², and Warwick Payten⁴

¹ Nuclear Fuel Cycle Research, NSTLI, Australian Nuclear Science and Technology Organisation, New Illawarra Road, Lucas Heights, Sydney, NSW 2234, Australia

² Formerly at Australian Nuclear Science and Technology Organisation, New Illawarra Road, Lucas Heights, Sydney, NSW 2234, Australia

³ School of Materials Science and Engineering, University of New South Wales, Sydney, Australia

⁴ NMDC, Australian Nuclear Science and Technology Organisation, Lucas Heights, Australia

Received: 27 March 2023

Accepted: 13 June 2023

Published online:

1 July 2023

© Crown 2023

ABSTRACT

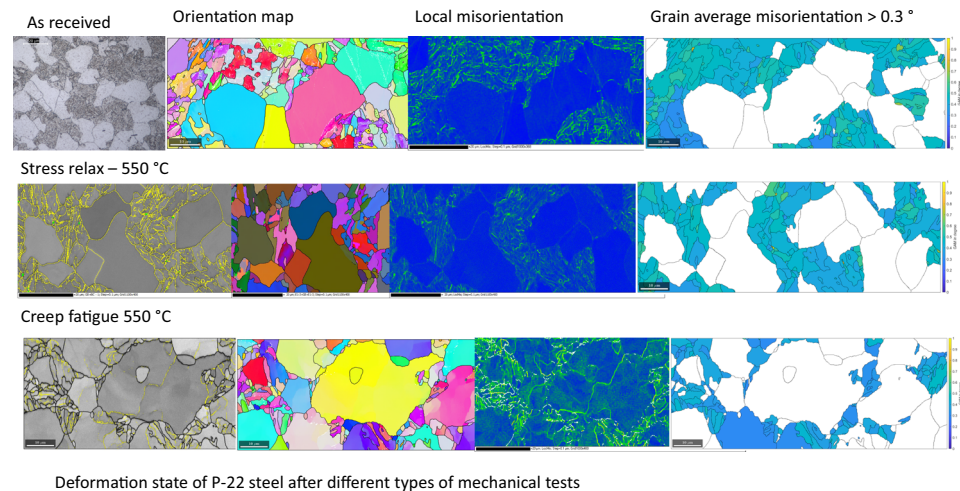
In this paper, the deformation mechanisms of a Fe–2.25%Cr–1%Mo (P22) steel are studied after tensile tests at room temperature (RT) and 550 °C (HT), creep-fatigue tests at 550 °C and stress relaxation test at 550 °C (HTSR). The RT, HT and HTSR tests produced permanent strain of about 2.5% by different processes. Deformation features such as the orientation of the grains, local misorientation, grain boundary type and distribution, etc., were characterized using electron backscatter diffraction. Transmission electron microscopy was done subsequently to obtain greater insight into the dislocation substructures. The as-received sample had a ferritic–bainitic microstructure, and a large amount of local misorientation was found in the bainite, indicating plastic strain due to phase transformation. After tensile strain to 2.5% at room temperature, the dislocations formed very small substructures (~100–200 nm) in the ferrite grains, and most of the retained plastic strain seemed to be concentrated in the bainite after deformation. Both the ferrite and bainite showed much lower local misorientation and dislocation wall content after a tensile test to 2.5% strain at 550 °C. Compared to the RT tensile sample, after creep-fatigue at 550 °C, the substructures in ferrite opened up considerably and formed small-angle grain boundaries, with clean areas as large as 20–25 μm. After stress relaxation at 550 °C, the ferrite displayed even less sub

Handling Editor: Megumi Kawasaki.

Address correspondence to E-mail: dhriti1@gmail.com; dhb@ansto.gov.au

structure, while the bainite seemed to have greater amounts of local misorientation than in the creep-fatigue case. However, the degree of misorientation was less pronounced than in the room temperature tensile case. These results have been discussed with respect to the causes behind the phenomena observed herein and their possible effects on mechanical behaviour.

GRAPHICAL ABSTRACT



Introduction

Creep-resistant Cr–Mo steels such as P22 are used extensively in power, refinery and chemical industries. This is a ferritic–bainitic steel which is used in the normalized and tempered condition. Cr increases the high-temperature strength and corrosion resistance, as well as improving the room temperature yield strength (YS) and ultimate tensile strength (UTS). Mo increases the YS, UTS, wear resistance and hardenability, while at the same time restraining grain growth and increasing creep resistance. The main application for this steel is in seamless pipes for high-temperature service [1]. It is also a candidate material for use in the lower temperature ranges inside very high-temperature reactors (VHTR) [2].

At high temperatures, as is well known, two time-dependent deformation mechanisms occur which cause a considerable amount of strain—(a) creep—which entails the increase in plastic strain under

constant load and (b) stress relaxation (SR)—resulting in a drop in stress under a constant constraint [3]. The interaction of creep with SR in combination with low cycle fatigue results in a majority of the damage in high-temperature conditions inside steam generation plants [4].

In this paper, the authors have endeavoured to perform an overall visual characterization using electron microscopic techniques and thereby obtain a phenomenological understanding of the deformation mechanisms in different samples of P22 steel that has experienced the same magnitude of permanent strain by different mechanical tests at room temperature and at 550 °C. The high-temperature deformation behaviour of ferritic/ferritic–pearlitic steels has been studied by some previous authors [5–7]. It was reported by Glover et al. in [5] that the effective stress reaches a maximum and remains practically constant in vacuum melted and zone-refined iron after a strain of about 1% is achieved at testing temperatures of 500–600 °C. This behaviour is related to the stress

level at these temperatures, and it was seen that at higher temperatures and lower stresses, the stress reached a peak value and then decreased at greater strains. Such behaviour in the stress–strain curve, where there is a plateauing tendency, as in the region of 500–600 °C, is thought to be typical of steels undergoing work hardening and recovery only, but with no recrystallization. The effect of alloying elements and temperature on recovery and recrystallization of hot-rolled low alloy steels has been investigated by Liang et al. [8]. They report that an increase in stress relaxation temperature decreases the time for initiation of recrystallization for a given alloy and, in general, speeds up the whole recrystallization process. Thus, at lower temperatures, the recovery process would be prolonged and would be the dominant mechanism for softening. This is in agreement with the work of Glover et al. mentioned above. They also found that alloying causes a delay in the onset of recrystallization, which they attribute to slower recovery due to interaction of dislocations with solute atoms.

A study of the effect of heavy warm deformation on the microstructure and texture of medium carbon steel by Storojeva et al. [7] was performed at temperatures 600–710 °C, where they found that ferrite softening was mostly due to continuous recrystallization. It would be noted that these temperatures are higher than those mentioned above.

One motivation for the present work was to provide some understanding of the reasons behind the significantly shorter remaining creep life after stress relaxation (SR) tests than expected in the previous studies in this steel [4, 9] as well as others [10]. The authors of these works reported that the creep life of the stress relaxation tested material was reduced by ~90% compared to the “virgin” material. However, optical micrographs did not demonstrate the amount of damage due to SR tests that would be expected to cause such a reduction in creep life [9]. Therefore, in this paper, more detailed characterization techniques were undertaken in order to elucidate the possible causes for this severe drop in creep life.

A creep-fatigue test sample was also characterized to compare the deformation microstructure to the other modes of testing studied here, viz. RT tensile, hot tensile and stress relaxation. This more complex mode was chosen as it is one of the damage mechanisms that high-temperature components undergo in power plants, including nuclear reactors. ANSTO has

a major research focus into damage mechanisms of Gen IV reactors, which can undergo creep-fatigue [11–14]. Since it has been shown that creep properties can be correlated with hot-tensile tests [15, 16], it is sensible to compare the microstructural manifestation of strain in samples deformed by these different types of tests after similar strain levels to assess the kind and degree of damage.

The distribution of dislocations, their organisation into dislocation walls and small-angle grain boundaries and the size and distribution of grains were studied using scanning and transmission electron microscopy (SEM and TEM) and electron backscatter diffraction (EBSD). These techniques were used in a complimentary manner so as to derive values for different parameters such as subgrain boundary misorientations, dislocation density in small-angle grain boundaries, etc., which could be used in phenomenological models for prediction of deformation mechanisms in these steels in future. In recent years, there have been numerous studies using EBSD to understand the deformation microstructure in various metallic alloys [17–21]. It should be noted that although some EBSD and TEM studies of strain localization have been performed on deformed dual-phase steels in recent years [19, 20, 22], there have not been systematic studies of the deformed, substructured and undeformed fractions of grains across different types of thermomechanical treatment, which the present paper aims to perform.

Experiments

The material tested was 2.25% Cr–1% Mo steel conforming to ASTM specification A387—Grade 22—Class 2. The test material was purchased by ANSTO from Van Leeuwen Eastern Australia Pty. Ltd., as 25-mm thick normalized and tempered steel plate. The as-received hardness was 200 HV.

The chemical composition of the test material (in wt%) is shown in Table 1.

The mechanical tests carried out on the Grade 22 steel samples were as follows: (a) tensile test at room temperature (RT) to 2.4% strain, (b) tensile test at 550 °C to 2.6% strain, (c) repeated stress relaxation tests at 550 °C and (d) creep-fatigue tests at 550 °C. This sets the homologous temperature, T_m at roughly 0.47–0.48.

RT tensile tests

The RT tests were carried out on an Instron® 5582 screw-driven test machine according to Australian Standard AS 1391–2005. The cylindrical test-pieces had nominal gauge dimensions of 8-mm ϕ and 48-mm length. The nominal strain rate was held constant at $7\text{e-}4/\text{s}$.

HT tensile tests

A second sample was prepared for hot-tensile testing, which was tested at 550 °C by applying a strain of up to 2.84%, which was ultimately relaxed to 2.5%.

Stress relaxation tests

The stress relaxation (SR) tests were performed on an Instron® 5582 screw-driven test machine in accordance with BS-EN-1:2003. The cylindrical test-pieces had gauge dimensions 8-mm ϕ and 100-mm length. The SR tests consisted of loading a sample at 550 °C ($\sim 0.45 T_m$) to 0.15% strain, holding at that strain for 1 week (168 h) and unloading completely within 30 s. The stress was recorded at regular intervals during the whole process. This cycle was repeated 23 times (excluding one test aborted due to power failure). The final permanent strain when unloaded was 2.5%. Further details of the stress relaxation experiment can be found in a previous publication by Humphries et al. [23, 24]. The total time at 550 °C was 3864 h.

Creep-fatigue tests

The creep-fatigue test was performed on an Instron 8561 servo-electric testing machine in accordance with ASTM E606 in strain control. The cylindrical test-piece had a gauge diameter of 6.35 mm. Uniaxial strain was measured by a capacitance extensometer directly fixed to the gauge section which was used to control the strain during the test. The cyclic part of the test was a symmetrical triangular waveform at a strain rate of $1.1\text{e-}4/\text{sec}$, and the strain amplitude was $\pm 0.5\%$, giving a total strain range of 1%. A 30-min hold was applied at the peak tensile strain of each cycle. Testing was stopped after 128 cycles.

From other creep-fatigue tests on the same steel, this was estimated to be about 1/3rd of the expected cycles to failure. The failure criterion generally used is a 6% drop from the linear trend of peak stress, which corresponds to the initiation of small cracks in the specimen. The total time at 550 °C was ~ 70.5 h.

Further details about the mechanical tests are summarized in Table 2. A more complete description of the details of the test conditions may be found in [23, 24].

The different exposure times in the SR and CF tests would have affected the degree of thermal ageing and also precipitate size, type and distribution (which would affect the resistance to dislocation motion).

Sample characterization

The samples for characterization were prepared from the cross-sections of the test specimens from near the centre. These were mechanically polished by diamond lapping film to 1- μm finish and then final polished with 0.05- μm colloidal silica to remove as much of the polishing-induced surface deformation as possible. The microstructure of P22 steel samples was characterized in the as-received, RT tested, creep-fatigue tested and stress relaxation tested conditions using a Zeiss® Ultra Plus™ scanning electron microscope (SEM) and a Jeol® 2200FS™ scanning transmission electron microscope (STEM). The grain orientations and local misorientation of the samples were characterized using electron backscatter diffraction (EBSD) with an Oxford Instruments® Nordlys™ detector and Aztec™ software. Data analysis for orientation information was done with Oxford Instruments® Channel 5 software. Further analysis of EBSD data was done using the MText plugin [25] for Matlab® in order to identify regions with high stored deformation such as those with high grain average misorientation (GAM) or grain orientation spread (GOS).

Table 1 Chemical composition of the Grade 22 steel

C	Mn	P	S	Si	Cr	Ni	Mo	Cu	Al	Sn	V	Fe
0.11	0.41	0.008	0.021	0.161	2.18	0.22	0.91	0.11	0.017	0.007	0.017	Bal.

Table 2 Test conditions of different samples of P22 steel

Test name	Temperature (K)	No. of cycles	Permanent strain (%)	Important stress values (MPa)
RT tensile	298	NA	2.4	0.2% PS = 508 MPa, Peak stress 563 MPa
HT tensile	823	NA	2.5	0.2% PS = 247 MPa, Peak stress 303 MPa
Stress relaxation at 0.15% strain for 168 h	823	23	2.5	Initial stress (N1) = 184 MPa Final stress (N1) = 43 MPa
Creep-fatigue at 1% strain range and 30 min hold at peak tensile stress	823	128		Stress at start of hold (N1) = 267 MPa Stress at end of hold (N1) = 142 MPa

Results and discussion

As-received sample

The microstructure of the as-received sample is presented in the SEM and optical micrographs in Fig. 1a and b, respectively, where large proeutectoid ferritic grains ($\sim 25 \mu\text{m}$) were present with some interspersed tempered upper bainite regions [24]. The bainitic regions consist of lath-like structures as seen in these images, but probably more clearly in the optical image. The dark field (DF) STEM micrograph in Fig. 1c shows that the bainite regions consist of “units” of the order of 0.5–1.25 μm , with carbide precipitates both at boundaries and inside the units. The apparently equiaxed “units” in Fig. 1c are most probably the cross-section of bainitic laths. The carbides on the lath boundaries (LB) were slightly larger with up to 300-nm length in some cases, while the intra-lath carbides had a maximum of about 200-nm length. Some basic EDS examination of the carbides was performed to determine their nature, which revealed that the precipitates in Fig. 1c and d are carbides of mainly Fe and Cr, with small amounts of other elements such as Mn, Ni, Mo, Si, etc. These samples are normalized and tempered at around 750 °C, and according to the work by Bacon and Nutting [26], as also reported by Hodgson et al. [27], the precipitates expected at these tempering temperatures include Fe₃C, Cr₇C₃, M₂₃C₆ and Mo₂C. However, according to our observations, the amount of Mo is only ~ 2 –2.5 at%, and the amount of Cr is less than that of C in all the precipitates examined. Moreover, the Fe/C ratio and M/C ratio were found

to be vary in most cases between 3 and 4, barring one exception, where it was found to be ~ 5 . (It has to be remembered that the C content cannot be determined too accurately using EDS, since it is a light element). Based on these observations, the precipitates can be said to mostly consist of Fe₃C and M₂₃C₆ type carbides. This assessment agrees with the observations made on the as-received samples in a study of the evolution of microstructure of the same material under creep conditions published previously [21].

The BF STEM micrograph in Fig. 1d shows that the ferrite grains are also dispersed with similarly sized, plate-like carbide precipitates, and have a moderate density of dislocations ($\sim 3 \times 10^{12}$ dislocations/m²). There are no visible dislocation “cells” at this scale. The inverse pole figure orientation map in Fig. 1e shows the bainite regions, having smaller grains and exhibiting greater orientation variations, between the larger, more uniformly coloured ferrite grains more clearly. Some unindexed points are seen along lines which are traces of polishing scratches. The local misorientation map in Fig. 1f gives an estimate of the average misorientation of individual pixels from the surrounding pixels and thus provides an insight into the extent of plastic deformation stored in a region. The local misorientation or kernel average misorientation provides a qualitative estimate of the dislocation density, as demonstrated through combined microscopic digital image correlation, EBSD and electron channelling contrast imaging (ECCI) by Rui et al. [18]. As can be observed clearly from this map, most of the ferrite grains have very low local misorientation (coloured blue), while most of the bainite regions have areas of relatively high local

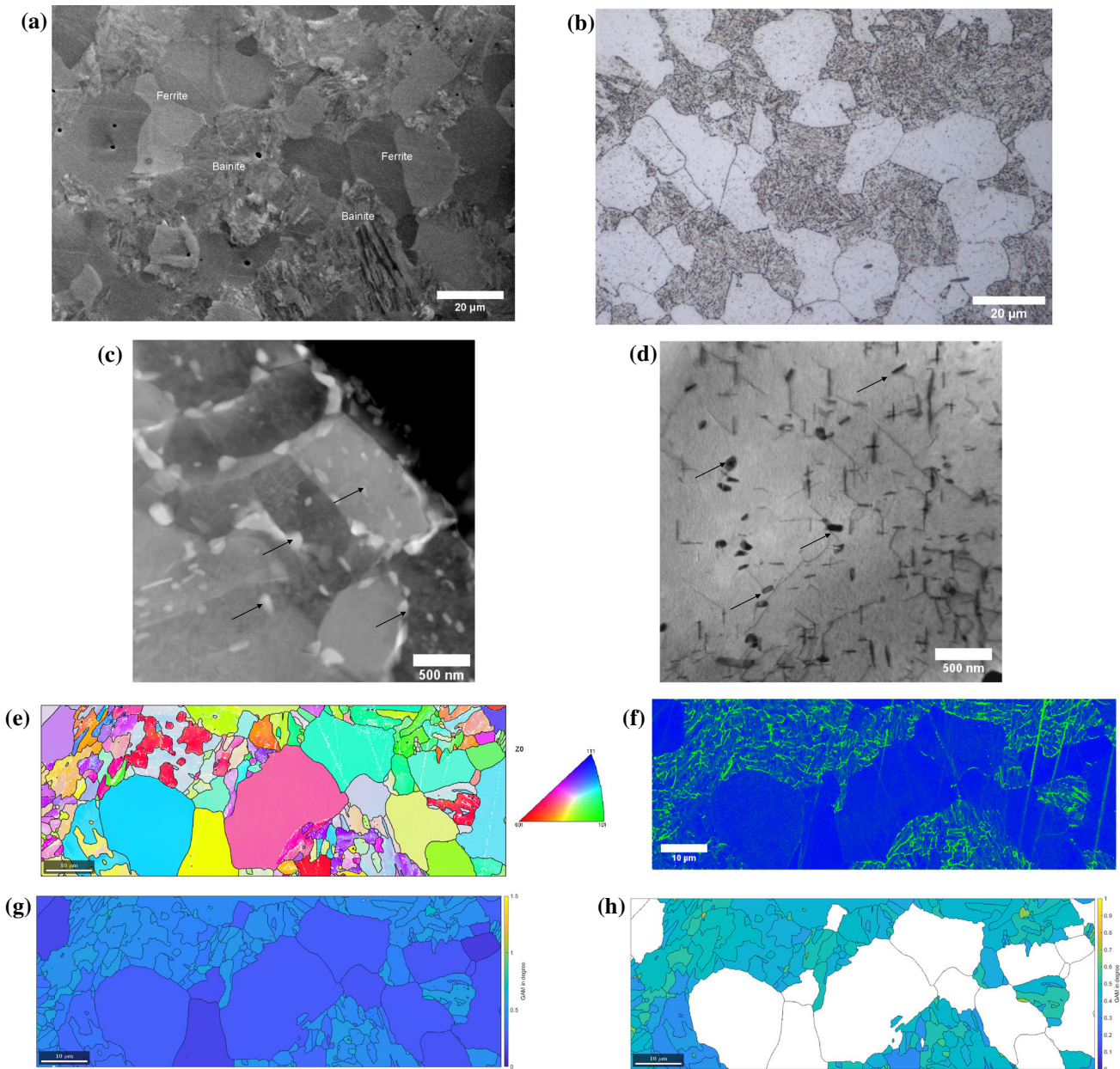


Figure 1 SEM image of an as-received sample of P22 steel showing a mixed microstructure—consisting of equiaxed ferrite grains and bainite with lenticular structure, as indicated by the labels, **b** optical micrograph of the as-received sample of P22 steel (etched in 2% Nital) and **c** DF STEM image showing bainite regions with lath boundaries and precipitates in as-received sample. In this image, the laths are likely visible in cross-section. Arrows show precipitates, most likely Fe₃C or M₂₃C₆ carbides, **d** BF STEM images of dislocation structure in the ferrite

of as-received sample, showing separate, randomly spaced dislocations in the ferrite grains. Arrows show precipitates, most likely Fe₃C or M₂₃C₆ carbides, **e** IPF map showing large equiaxed grains in ferrite and small, elongated regions in bainite. **f** Local misorientation map showing ferrite grains mostly free of small-angle grain boundaries (range: 0–2°), **g** grain average misorientation (GAM) showing average kernel misorientation within each grain and **h** grains with GAM > 0.3°—threshold above which only bainite grains exist in the as-received sample.

misorientation (green-/yellow-coloured lines). This is shown more quantitatively in Fig. 1g which maps the average kernel misorientation within each grain or grain average misorientation (GAM). Here, it is clear

that the bainite regions, which have a light blue to light green colour, have higher GAM values than the ferrite grains, shown in deeper blue. If the map is thresholded by GAM values, as presented in Fig. 1h,

it is seen that almost all of the regions above $GAM > 0.3^\circ$ consist of bainite.

The EBSD maps in Fig. 2 show the same regions coloured according to the “recrystallized fraction” (this terminology is used in accordance with the usage in the AztecTM software) classification based on the misorientation within each grain. Individual grains have been delineated by black boundaries (misorientation across pixels $> 7.5^\circ$). The grains have been classified as deformed ($> 1^\circ$ average misorientation between pixels within grain), substructured (pixel to pixel average misorientation within grain $< 1^\circ$ but misorientation between subgrains $> 1^\circ$) and undeformed (average misorientation within grain $< 1^\circ$ and no subgrains). As can be seen from the histogram of the complete map (Fig. 2a), the fraction of recrystallized grains (F_{Rex}) = 37%, fraction of substructured grains (F_{Sub}) = 62% and fraction of deformed grains (F_{Def}) = 1%. When the full dataset is split into a bainite (Fig. 2b) and a ferrite (Fig. 2c) subset, it is clearly seen that the bainite has larger fraction of substructured and deformed grains (95% substructured and 1% deformed), while the ferrite phase has more undeformed or substructured grains (62% undeformed and 38% substructured) and almost no “deformed” grains. The same information can be seen in a slightly different manner in the form of subgrain boundary density (SGBD) maps, where the length of the subgrain boundaries divided by the grain area is plotted for each grain, as shown in Fig. 2d. Again, the bainite areas show a higher SGBD value than ferrite. This becomes clearer when the areas of SGBD higher than 1 are plotted—only bainite areas become highlighted when such a criterion is used.

This shows that most of the dislocations in the as-received material are present in the bainite structure, in the form of small-angle grain boundaries and stored deformation, with the ferrite almost strain free. This observation is in agreement with those of He et al., who show that bainite has a high density of dislocations and small-angle grain boundaries compared to ferrite in a completely ferritic steel [28]. The higher dislocation content and stored deformation is likely to be the result of transformation stresses induced during the formation of the bainite.

Room temperature tensile test (RTT)

The grain structure in the RT tensile sample is clearly visible in the IPF map in Fig. 3a, which shows subtle variations in colour, or, equivalently, orientation, even in large ferrite grains, indicative of stored deformation. In the band contrast image in Fig. 3b, the microstructure of the room temperature deformed (2.4% strain) sample is shown, along with 1° subgrain boundaries. It is clear from the contrast variations and regions with yellow specks or broken lines that the ferrite grains do not have a clean structure in this sample, as compared to the as-received sample. A map showing deviations from the mean grain orientation or grain orientation spread (not shown here due to lack of space) also demonstrates the same point. This is indicative of the deformation, the ferrite grains have undergone. The EBSD-generated local misorientation map of the RT deformed sample in Fig. 3c shows that there is a much higher degree of local misorientation in this sample than in the as-received sample (Blue—low, green—medium and red—high misorientation). The bainite areas exhibit much higher density of local misorientation lines than the ferrite areas, as indicated by the denser population of green lines in the bainite regions compared to the ferrite grains. This is probably due to the fact that the dislocations in the bainite have organized themselves into walls creating $\sim 1^\circ$ subgrain boundaries (as shown in Fig. 3a), while those in the ferrite are more randomly distributed. The large grains of ferrite also show networks of green lines with higher local misorientation than in the as-received sample. The high magnification EBSD map in Fig. 3d shows the local misorientation of a small area from the map shown in Fig. 3c, marked with a dashed square in that figure. At the bottom of the image in Fig. 3d, a group of lines with high misorientation angles is seen emanating from the grain boundary going almost vertically from the centre of the bottom edge of the picture. The grain boundary map in Fig. 3e showing boundaries with misorientation $> 0.5^\circ$ corresponds well with the local misorientation map. This shows that the lines of high local misorientation are related to small-angle grain boundaries. The bright field (BF) STEM image in Fig. 3f shows similar network structures in the ferrite grains at higher magnification, indicating that the small-angle grain boundaries seen in the EBSD maps, with relatively high local misorientation, consist of

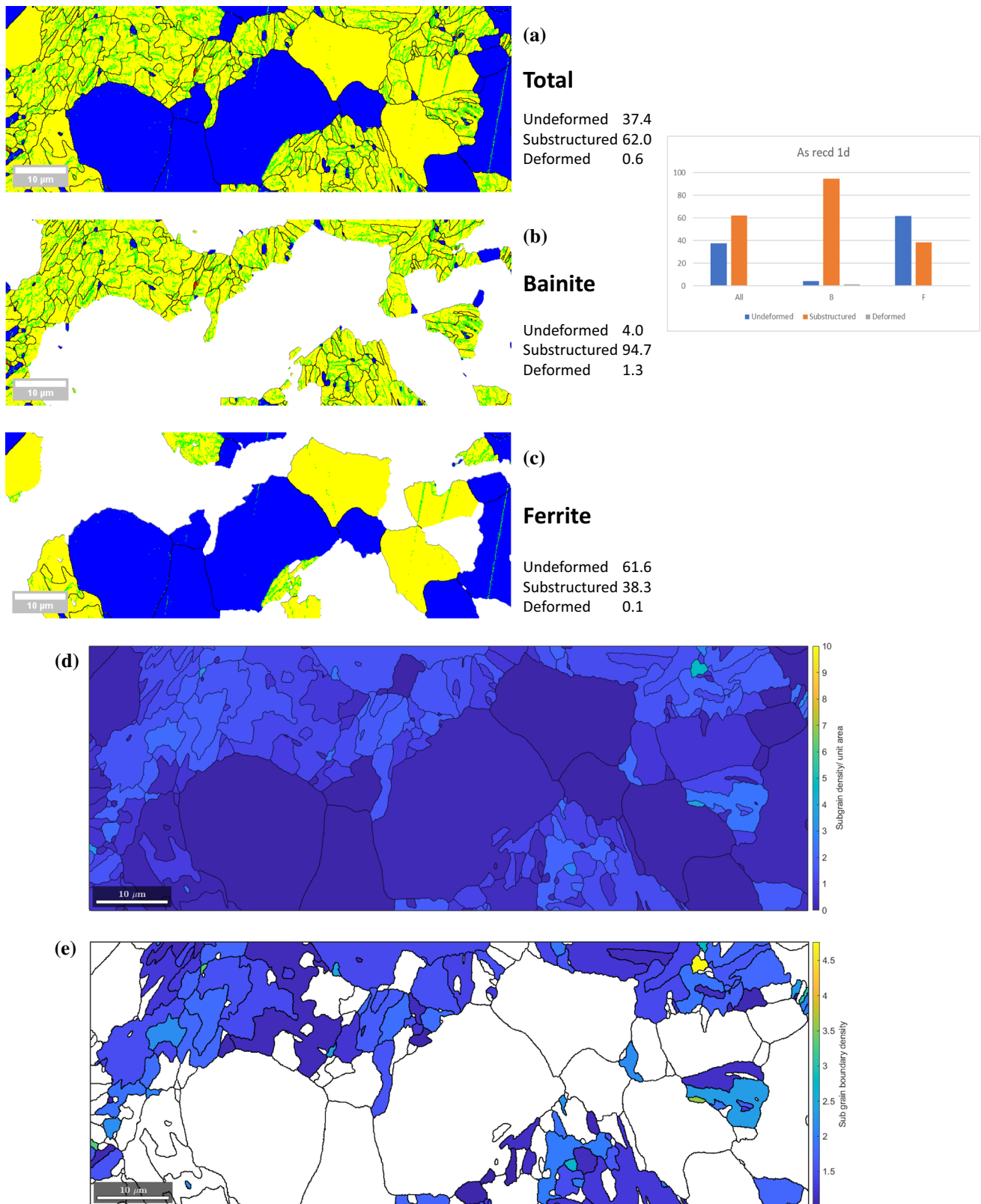


Figure 2 Undeformed, substructured and deformed fraction—*a* as-received sample—*a* total area, *b* bainite, *c* ferrite, *d* subgrain boundary density map—length of subgrain boundary segments

divided by grain area and *e* subgrain boundary density map showing that areas with SGBD > 1 consist almost exclusively of bainite regions.

dislocation walls. The BF STEM image in Fig. 3g shows a comparison between a portion of the local misorientation EBSD map and a BF STEM image, indicating the network of small high local misorientation lines and a similar dislocation “cluster” or “wall” emanating from a grain boundary. Thus, from the local misorientation map and the BF STEM image, it is clear that the subgrain boundaries tend to emanate preferentially from prior α (ferrite) grain boundaries. The thresholded EBSD map in Fig. 3h shows the areas with GAM greater than 0.3° , and in this case, these areas include both ferrite and bainite regions, unlike in the as-received case, where only bainite regions had the higher GAM values. However, even here, the ferrite grains having $\text{GAM} > 1^\circ$ have lower GAM values than bainite regions in the same category. The STEM BF image in Fig. 3i shows dislocation walls forming subgrains within the bainite phase, which are about 500 nm (or smaller) in size, consistent with the bainite regions in the EBSD map in Fig. 3c and e. In summary, while the bainite regions have a uniformly high distribution of small-angle grain boundaries (SAGBs), the ferrite regions have a higher density of SAGBs near prior α GBs, with the interiors having more of randomly distributed dislocations. Whether a grain is considered “substructured” or “deformed” in the EBSD maps, depends not as much on the population of such SAGBs, but more so on whether the misorientation angle across the individual SAGB is larger than an arbitrary threshold (here fixed at 1°), even if there is a single such boundary. This will have a strong effect on the fractions of these regions, as evident in the next paragraph.

The EBSD “recrystallized fraction” map in Fig. 4a shows the distribution of the deformed, substructured and undeformed grains inside the total area scanned in the RT tensile (2.3% strain) deformed sample. Here, it is clear that the fractions of deformed and substructured grains have increased compared to the as-received sample, and that of the undeformed have decreased. The EBSD maps show that the bainite regions in Fig. 4b have a higher fraction of deformed “grains” or domains (5%) compared to undeformed grains (3%) and substructured grains consist of a majority (92%). Similar analysis on the ferrite grains in Fig. 4c shows that most of these ($\sim 98\%$) are “substructured” and $< 0.5\%$ are deformed. Thus, it is confirmed from this analysis, that both bainite and ferrite show an increase in

dislocation density compared to the as-received structure, as expected. However, while the major shift in ferrite is from “undeformed” to substructured (AR- undeformed 62% and substructured 38%; tensile—undeformed 1% and substructured 98%), there is no significant shift in bainite except for a small change from substructured to deformed (AR—Subs = 95% and Def. = 1%; tensile—Subs. = 92% and Def. = 5%). The higher concentration of local misorientation in the bainite regions may be due to their higher initial dislocation density and the smaller “grain” size than ferrite, which prevents dislocation motion to form a well-distributed network. This observation is also in accordance with the observations on bainitic and ferritic steels shown in [28].

On the other hand, the ferrite grains have large areas which have relatively low dislocation content, with dislocations organized in networks creating small-angle grain boundaries. These networks separate the ferrite grains into subgrains. However, it is also clear that the overall dislocation density has increased in both ferrite and bainite, as compared to the as-received sample, as expected.

High-temperature tensile test at 550 °C (HTT)

The hot-tensile sample was scanned using EBSD by a similar procedure as the other samples, and the results are presented in Fig. 5. The IPF map shows the overall grain structure in Fig. 5a, while the BC map shows the small-angle grain boundaries ($1^\circ < \theta < 7.5^\circ$, yellow) and the large angle grain boundaries ($> 7.5^\circ$, black) in Fig. 5b. It is clear that the ferrite grains are almost devoid of subgrain boundaries, and almost the entire population of SAGB are present in the bainite regions. This fact is emphasized by the local area misorientation map in Fig. 5c, which shows most of the high intensity of misorientation in the bainite regions. As further evidence, when the map is thresholded into regions of $\text{GAM} > 0.3^\circ$, as shown in Fig. 5d, only the bainite areas become highlighted, similar to the as-received case, and unlike the RT tensile sample.

The undeformed, substructured and deformed fractions for the hot-tensile sample in the overall area, the bainite and the ferrite regions are shown in Fig. 6a, b and c, respectively. In this sample, almost all of the bainite and ferrite regions are substructured, with a small area appearing undeformed in

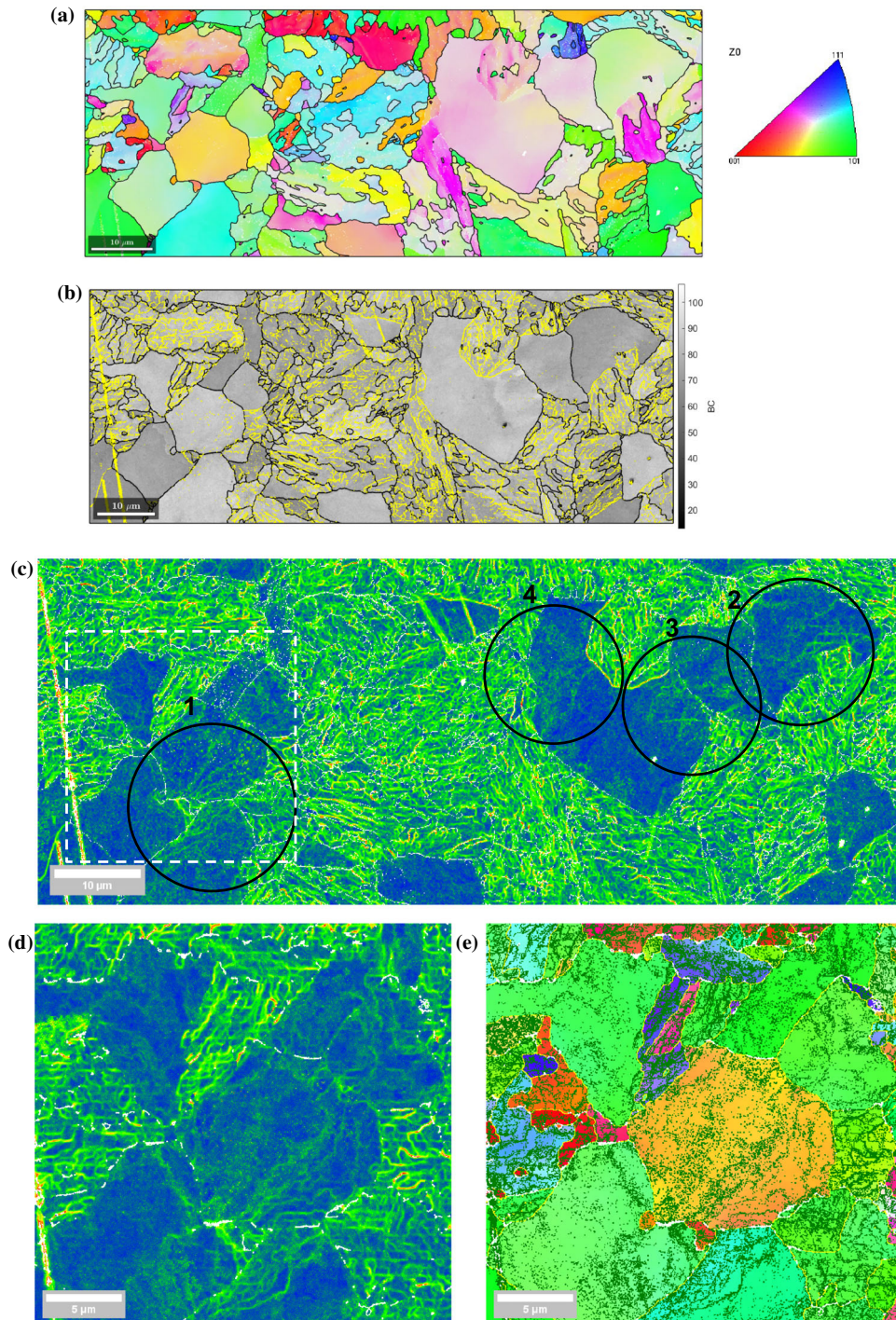


Figure 3 **a** IPF map of RT tensile sample showing subtle variations in colour (orientation) even in large ferrite grains, **b** RT tensile test up to 2.3% strain—band contrast map with 1° grain boundaries, **c** local misorientation map showing the highly deformed structure in the bainite, and the ferrite grains showing networks of small-angle grain boundaries and dislocation walls (circled) in RT tensile sample, **d** local misorientation map showing the network of small-angle grain boundaries and dislocation substructure in ferrite, **e** IPF map with small-angle grain

boundaries ($> 0.5^\circ$) marked dark green showing very good correspondence with the local misorientation map, **f** BF STEM image showing almost interconnected dislocation wall network ($\sim 200\text{--}500$ nm cell size), **g** EBSD local misorientation map and BF stem image showing dislocation walls emanating from ferrite grain boundaries in RT tensile sample, **h** map of RT tensile sample with areas having grains with $\text{GAM} > 0.3^\circ$ —which include both ferrite and bainite grains and (i) dislocation walls inside bainite showing subgrain formation (subgrain size < 500 nm).

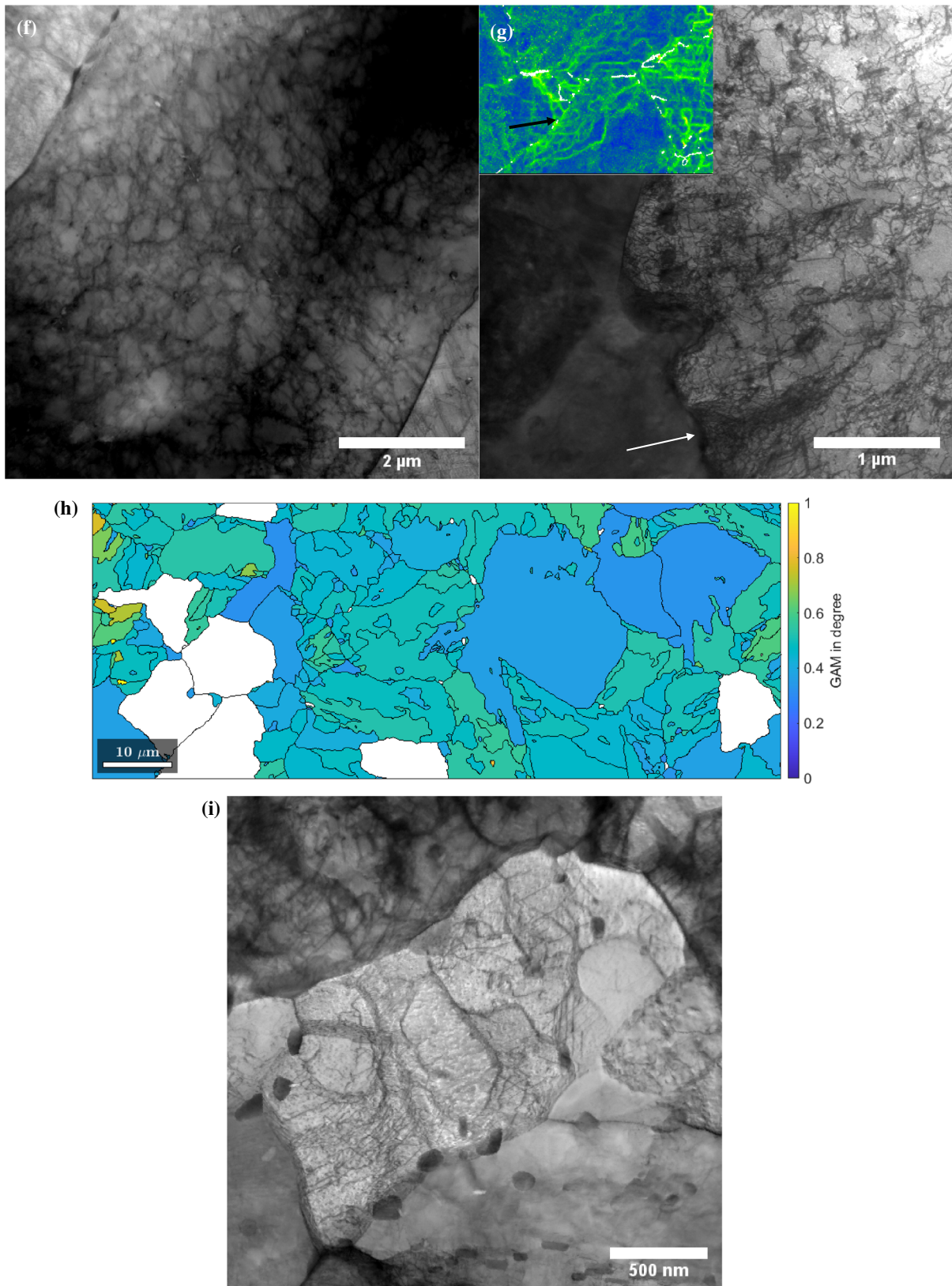


Figure 3 continued.

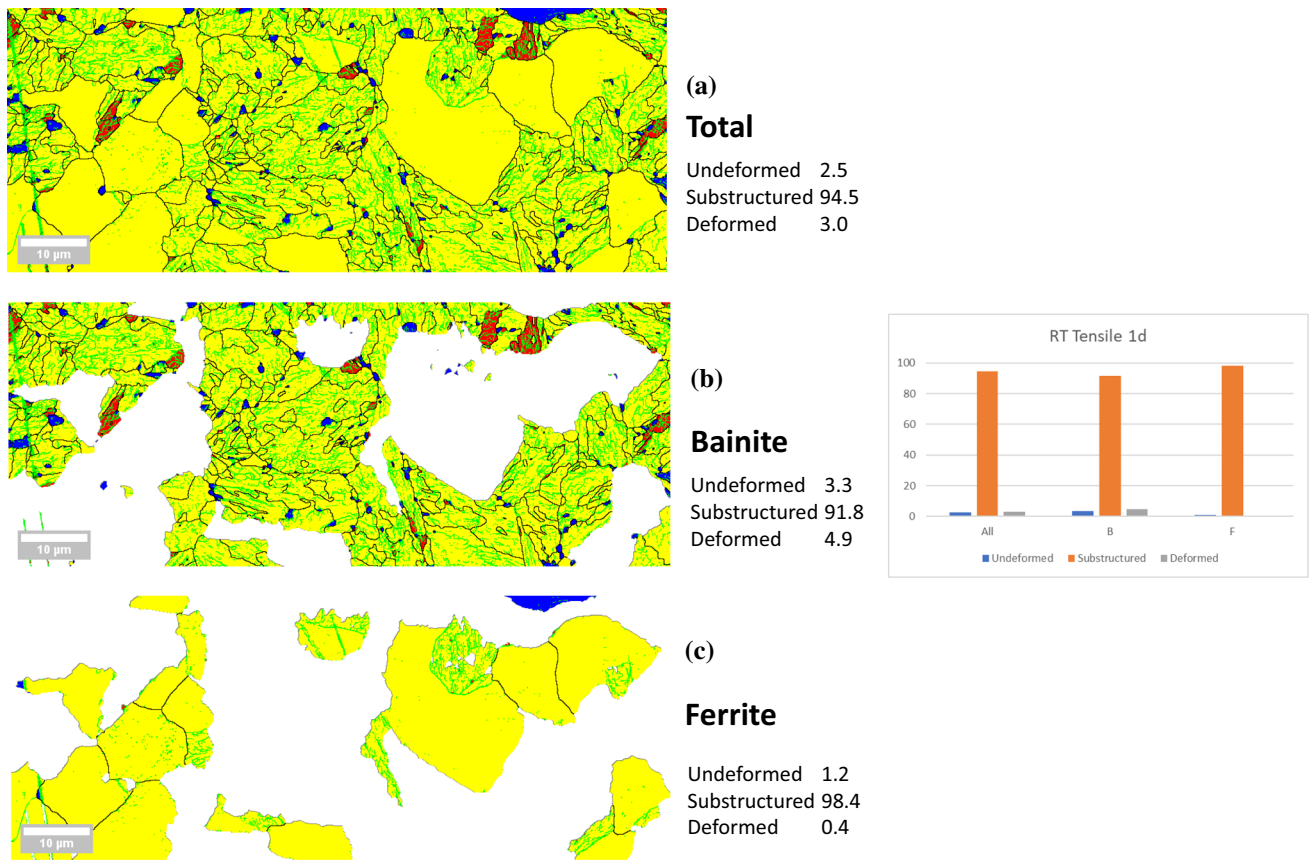


Figure 4 Undeformed, substructured and deformed fraction—RT tensile sample—a total area, b bainite area and c ferrite area.

both phases. The “substructured” nature of the ferrite may be somewhat misleading, as a 1° grain boundary (GB) map shows that in many grains, there is a very short segment of a small-angle grain boundary (SAGB) in a corner of the grain, which causes it to be described as a substructured grain. This means that the dislocations have been driven out of the α grains to a large extent, except for a small fraction which has formed SAGBs within a small region of the grain. Thus, most of the ferrite could actually be classified as “undeformed”, except for small regions near the grain boundaries. This is in fact confirmed by the GAM map in Fig. 5d, which shows that all the ferrite grains have lower local misorientation than 0.3° , the same value as in the as-received sample. The removal of dislocations and expansion of subgrains similar to the phenomena observed in P92 steel, albeit at slightly higher temperatures (600–700 °C), which was attributed to climb of edge dislocations over precipitates [29]. As the present alloy, P22, has lower concentrations of solute than P91, it is possible that mechanisms involving dislocation motion, including

climb, may become active at lower temperatures in this case, since it is well known that solute atoms hinder dislocation movement [30, 31]. This can happen both because of the solute drag effect and lowering of the stacking fault energy which reduces the tendency for cross-slip, thus making recovery more difficult in alloys with higher solute concentrations. Only the bainite shows some deformed fraction. There is almost no spheroidization of the bainite due to the hot-tensile test at 550 °C, as evident from the EBSD images.

High-temperature stress relaxation test (SR)

The stress relaxation test was carried out at 550 °C, and the sample was taken to a strain of 0.15% for 23 cycles, while the total strain was 2.5% after unloading, as mentioned in the experimental section. The EBSD IPF-Z map in Fig. 7a shows the general grain structure of the scanned area, while the local area misorientation map in Fig. 7b shows the accumulation of plastic strain in the form of dislocation walls. Figure 7b shows that most of the large ferrite grains

have very low internal local misorientation, while the bainite regions have curving lines with relatively high local misorientation. This observation is confirmed by the 1° grain boundary map in Fig. 7c, where inside the bainite regions, a high population of small-angle grain boundaries is visible. The GAM map with a 0.3° threshold again shows that the regions with $\text{GAM} > 0.3^\circ$ include only bainite areas, consistent with the SAGB map in Fig. 7c.

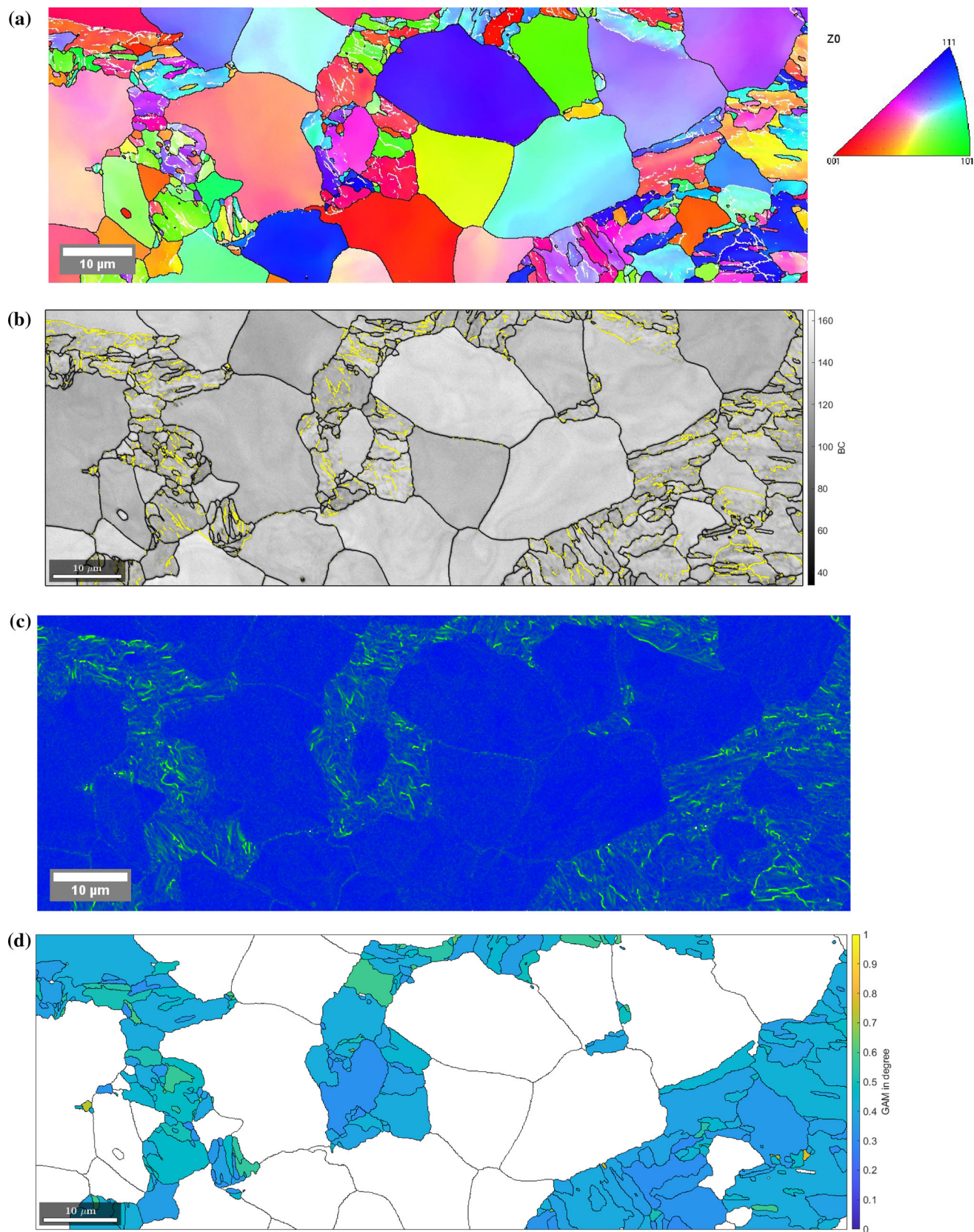
The recrystallized fraction map in Fig. 8a shows that in the area scanned, 56% area is “undeformed” and $\sim 43\%$ area is “substructured”. Further analysis shows that in the bainite areas, $\sim 94\%$ area is “substructured” (Fig. 8b), while in the ferrite areas, $\sim 96\%$ is “undeformed” (Fig. 8c). There is negligible “deformed” area in the scanned region ($< 1\%$) and is observed only in the bainite. This is in sharp contrast to the RT tensile sample, where there was $\sim 49\%$ substructured and $\sim 49\%$ deformed area overall, with the ferrite being $\sim 94\%$ substructured and the bainite $\sim 77\%$ deformed. Thus, the stress relaxation cycles at 550°C effectively removed any sign of the appreciable plastic strain that is applied through the whole process. The BF TEM images in Fig. 8d and e show two areas which show very little dislocation activity in the ferrite and are thus consistent with the EBSD images. The observations are consistent with dynamic recovery occurring during the long exposure to intermediate temperature under stress during the HTSR cycles. This is consistent with the idea that dynamic recovery is the primary mechanism for dynamic restoration of properties for α -ferrite due to its high stacking fault energy [32]. This is possible at the relatively low strain of 2.5% because of the intermediate deformation temperature of 550°C , since the strain required for recovery decreases with increasing working temperature [32]. The black dot and streak-like features in the TEM micrographs are carbide precipitates.

In the HTSR tests, the initial stress varied from 183 to 191 MPa at the beginning of each cycle and the final stress varied from 42 to 62 MPa at the end of each cycle. Since the modulus is about 160 GPa, the ratio σ/E varied from $\sim 9.5 \times 10^{-4}$ to 2.5×10^{-4} . Since the homologous temperature, T/T_m , was ~ 0.47 – 0.48 , these stress ranges put the test in the transition regime of dislocation creep and Coble (grain boundary diffusion) creep, as determined from Ashby maps. The TEM images in Fig. 1(d) and Fig. 8d and e also show that the carbide precipitates

have changed little in size and shape from the as-received condition and at the same time make it clear that the dislocation density has decreased visibly after the SR test.

Creep-fatigue test at 550°C (CF)

As mentioned in the experimental section above, the P22 steel samples were tested under creep-fatigue conditions at 550°C for 128 cycles to a strain-amplitude of 1%. The IPF map in Fig. 9a shows the sample Z direction orientations and grain boundaries ($> 7.5^\circ$) overlaid on them. The EBSD map in Fig. 9b shows a band contrast map with grain boundaries, as well as SAGBs $> 1^\circ$ misorientation as yellow lines. It is clear that the ferrite grains have large areas separated by low-angle grain boundaries, as indicated by the arrows. The local misorientation map of the same area in Fig. 9c shows that the bainite areas have high local misorientation, especially between bainite subgrains. However, in the creep-fatigue test sample examined here, it is also clear that the ferrite grains have large areas of relatively low local misorientation separated by well-arranged subgrain boundaries (circled and marked with an arrow in Fig. 9c), corresponding to lines of relatively high local misorientation. This is different from the RT tensile samples, where the ferrite had small subgrain boundaries close to each other, with subgrain sizes of the order of 200 nm. The subgrains in the ferrite regions in the creep-fatigue sample are much larger (5–20 μm). The recrystallized fraction map in Fig. 10a shows that $\sim 88\%$ of the total area is seen as substructured, while only 12% is undeformed and almost no area is deformed. The GAM map showing areas with $\text{GAM} > 0.3^\circ$ in Fig. 9d also shows that the local misorientation can be high even in ferrite regions, as evident in some grains (blue) at the bottom of the figure. These observations are consistent with reorganization of dislocations into subgrain walls as observed during creep [33], which is likely to be a dominating factor in the determination of the final microstructure as out of the ~ 70.5 h at 550°C , about 64-h duration was at constant strain at 1% strain. Even the loading was performed at a quasi-static strain rate of $1.1 \times 10^{-4}/\text{s}$. Other researchers have observed a decrease in dislocation density and formation of subgrain boundaries in creep-fatigue tests as well, for example in Alloy 617 [34], where the authors reported very low dislocation densities



◀ **Figure 5** Hot-tensile sample tested at 550 °C. **a** EBSD IPF (Z) map, **b** band contrast map with grain boundaries (yellow GB: misorientation > 1° and black GB: misorientation > 7.5°), **c** hot-tensile sample tested at 550 °C—local misorientation map and **d** areas with GAM > 0.3°—these include mostly bainite regions.

inside the subgrain boundaries. A decrease in dislocation density and coarsening of subgrain size was also observed after creep-fatigue on a P91 steel [35].

A further analysis of the area shows that both the ferrite and the bainite areas have a majority of the grains deemed to be substructured, with a small fraction undeformed. These observations again indicate that the ferrite has undergone dynamic recovery to the extent that there are very large cells with sizes of the order of the grains.

The TEM images in Fig. 11a and b show a small-angle grain boundary in the creep-fatigue sample in detail. The dislocations constituting the grain boundary are clearly visible in Fig. 11b. Further analysis of TEM images from another small-angle grain boundary in Fig. 11c and d showed that the

distance between the dislocations was ~ 16 nm. The relationship between the (edge) dislocation distance and the angle of misorientation across the small-angle grain boundary (tilt) is given by $\sin(\theta/2) = b/2d$ or $\theta \approx b/d$ (when $b/d \ll 1$) [36] where θ = grain boundary misorientation angle, b is the Burgers vector magnitude and d = distance between adjacent dislocations.

Knowing the Burgers vector for $\frac{1}{2} \langle 111 \rangle$ dislocations in ferrite, which is ~ 2.47 Å, this yields a misorientation of ~ 0.9°, when all dislocations are considered to be of edge character. Using convergent beam electron diffraction (CBED) patterns from the left and right side of the grain boundary, as shown in Fig. 11e and f, the misorientation across such a grain boundary was estimated to be about 0.5–0.8°. (This was estimated by measuring the angular displacement of the particular zone axis shown by the blue and red arrows, respectively, in Fig. 11e and f, respectively). This is reasonably close to that estimated from the dislocation distance analysis. This value of misorientation across the subgrain

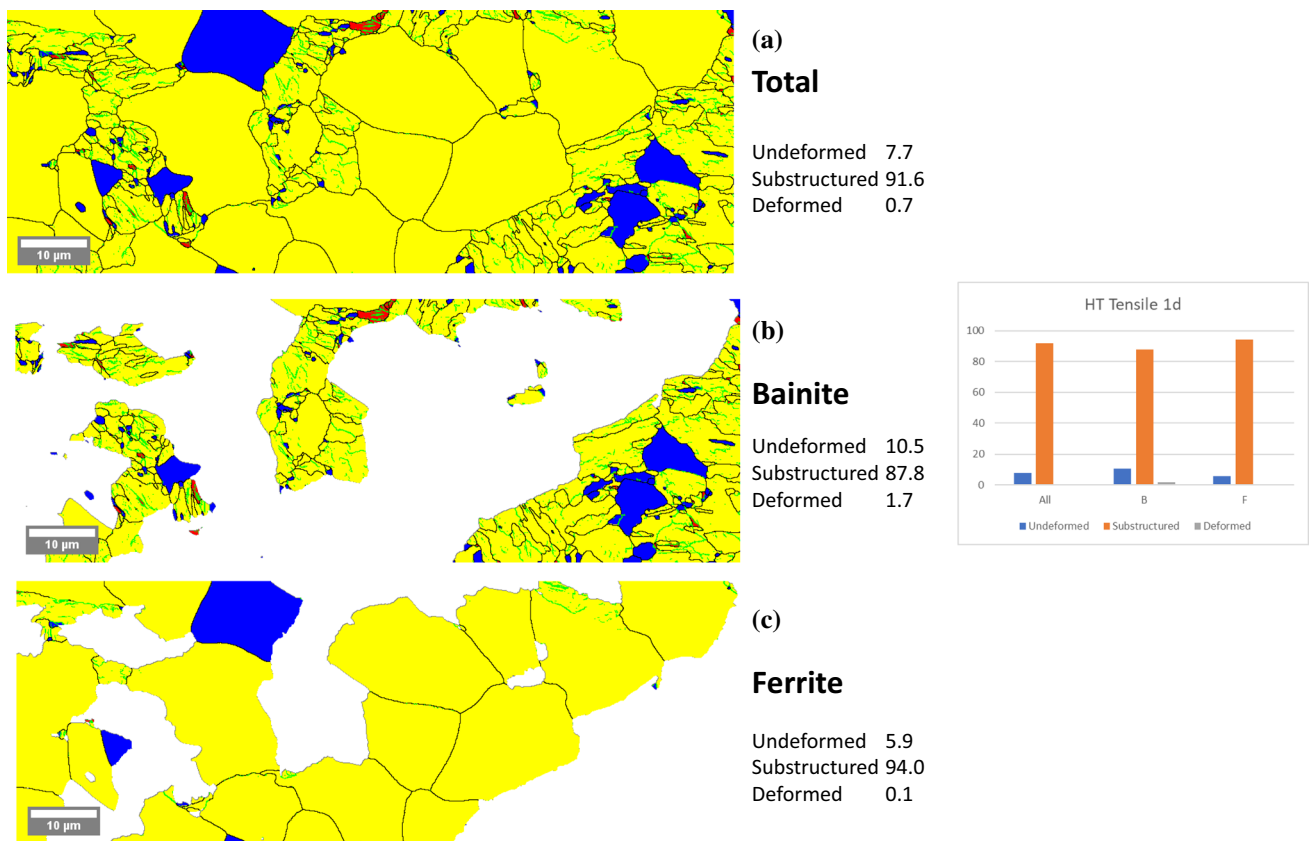


Figure 6 Hot-tensile sample tested at 550 °C—recrystallized fraction for **a** total, **b** bainite and **c** ferrite.

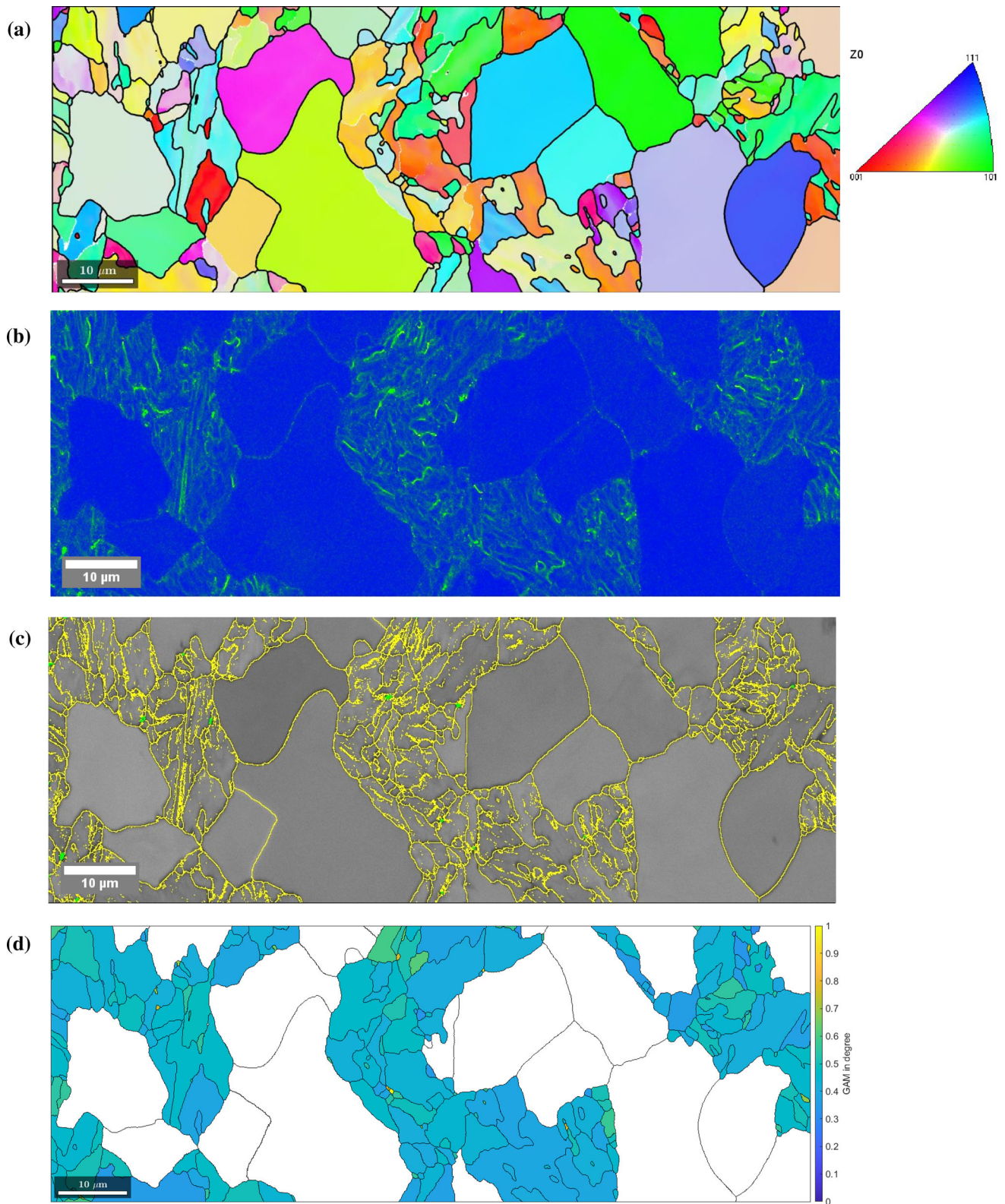


Figure 7 High-temperature stress relaxation test sample—550 °C, 2.5% permanent strain, 23 cycles, **a** IPF-Z map showing general grain structure, **b** local misorientation map showing almost no

stored deformation in the ferrite grains, **c** grain boundary map showing GB for misorientation > 1° and **d** areas with GAM > 0.3° include only bainite regions.

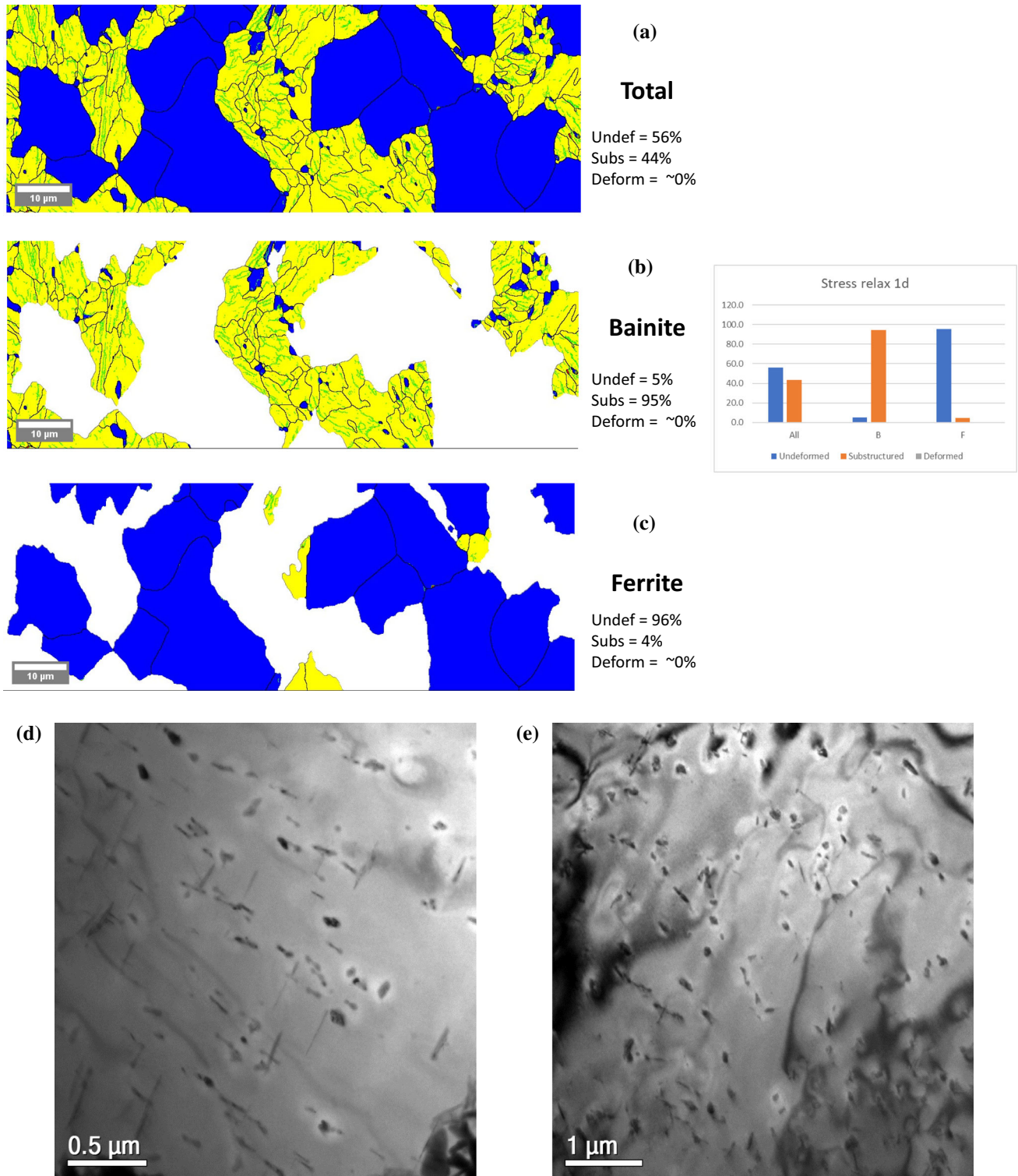
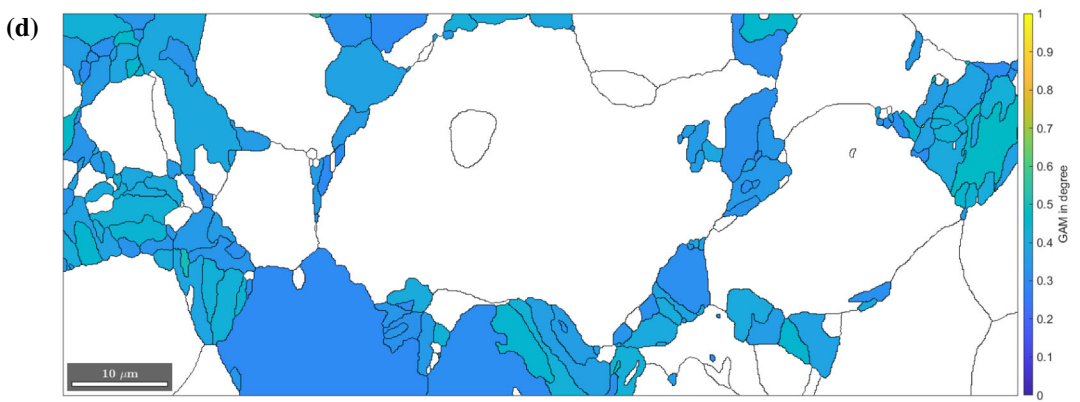
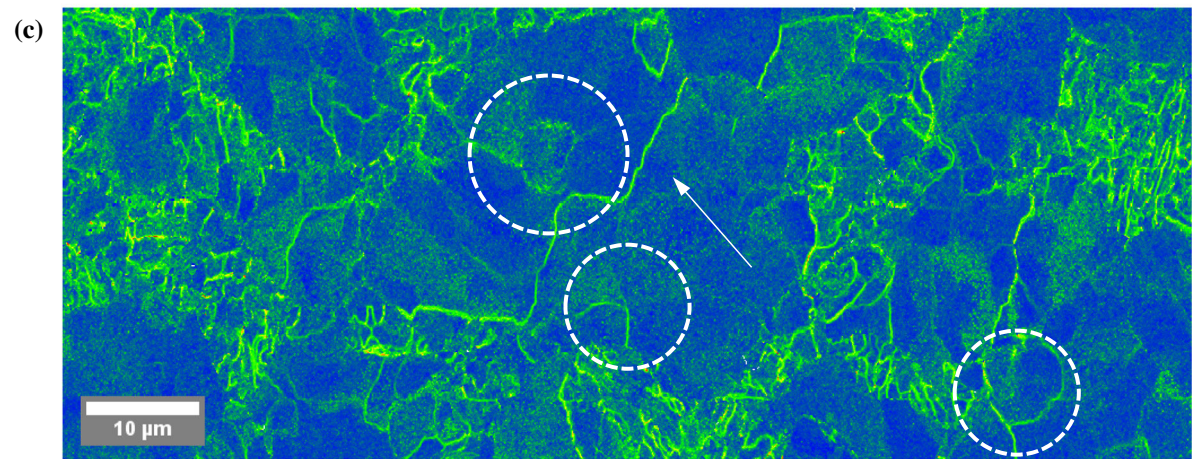
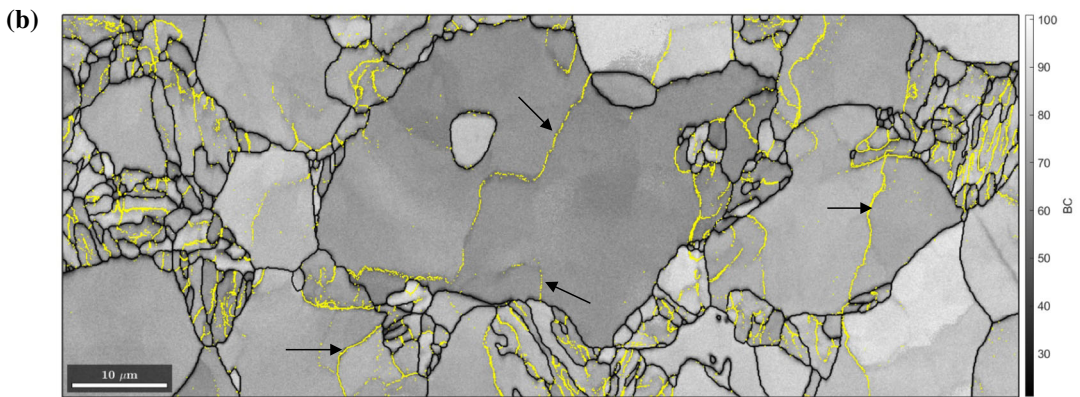
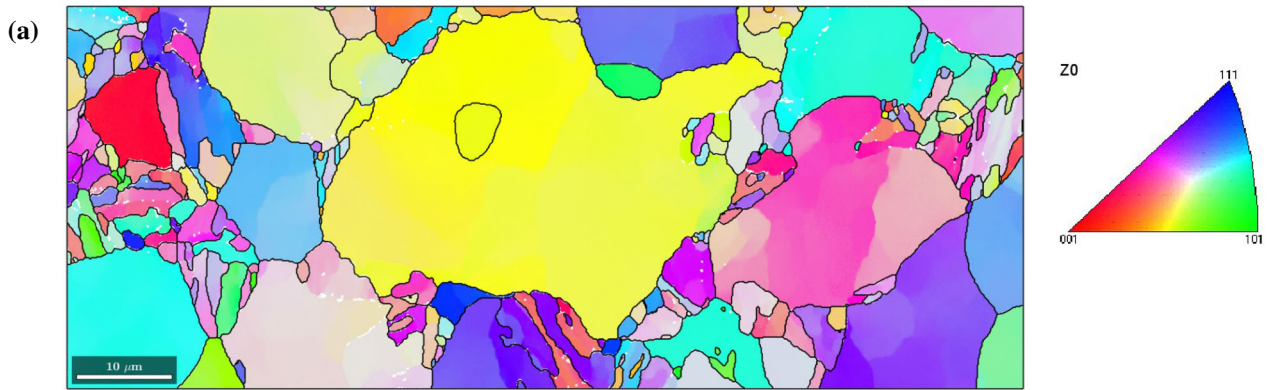


Figure 8 Recrystallized fraction map of the HT stress-relaxed sample—**a** total, **b** bainite and **c** ferrite, **d** and **e** BF TEM images of the 550 °C stress-relaxed sample showing little dislocation

activity in the ferrite grains and very little change in the size and distribution of the carbide precipitates (dark spot-like and streak-like features).



◀ **Figure 9** Creep-fatigue (550 °C) sample EBSD maps (a) IPF map showing grain orientations with GB > 5° and subgrain boundaries > 0.5°, (b) band contrast map with subgrain boundaries > 1° and grain boundaries > 7.5°, and (c) local misorientation map showing ferrite grains with large clean areas separated by lines of relatively high local misorientation, the bainite areas interspersed between the ferrite grains, and with much higher density of local misorientation lines. The interior of ferrite grains shows randomly dispersed points of slightly high local misorientation, but not forming any clear boundary, (d) Areas with GAM > 0.3° include mostly bainite areas, but also some ferrite grains.

boundaries is also close to that obtained from EBSD analysis of the subgrain boundaries for this sample.

Comparison of deformation microstructures

The data on the undeformed, substructured and deformed fractions for all the samples are summarized in Tables 3a (total area), 3(b) ferrite phase area and 3(c) bainite phase area, rounded to the nearest

0.5%. The same data are also presented in the form of bar charts in Fig. 12a, b and c.

It is clear from the tables and the plots that in all the samples, the bainite phase has more deformed fraction than the ferrite phase.

From these observations, it is clearly seen that the RT tensile sample has the greatest fraction of deformed crystals, and this fraction decreases to negligible amounts (< 1%) in the hot-tensile, stress relaxation and creep-fatigue samples. The RT tensile sample has the highest fraction of substructured grains in the ferrite phase (98%) followed by creep-fatigue and the hot-tensile sample (90–96%). The stress relaxation sample shows the highest fraction of undeformed (“recrystallized” according to the HKL® software) grains—56%—among the deformed samples, greater even than the as-received sample (38%), while the RT tensile sample has the least (~2.5%). The ferrite in the SR sample has the highest amount of undeformed fraction—96%. Thus, it appears that the process of stress relaxation under these conditions (550 °C, 168 h holding at 0.15% strain, 23 cycles)

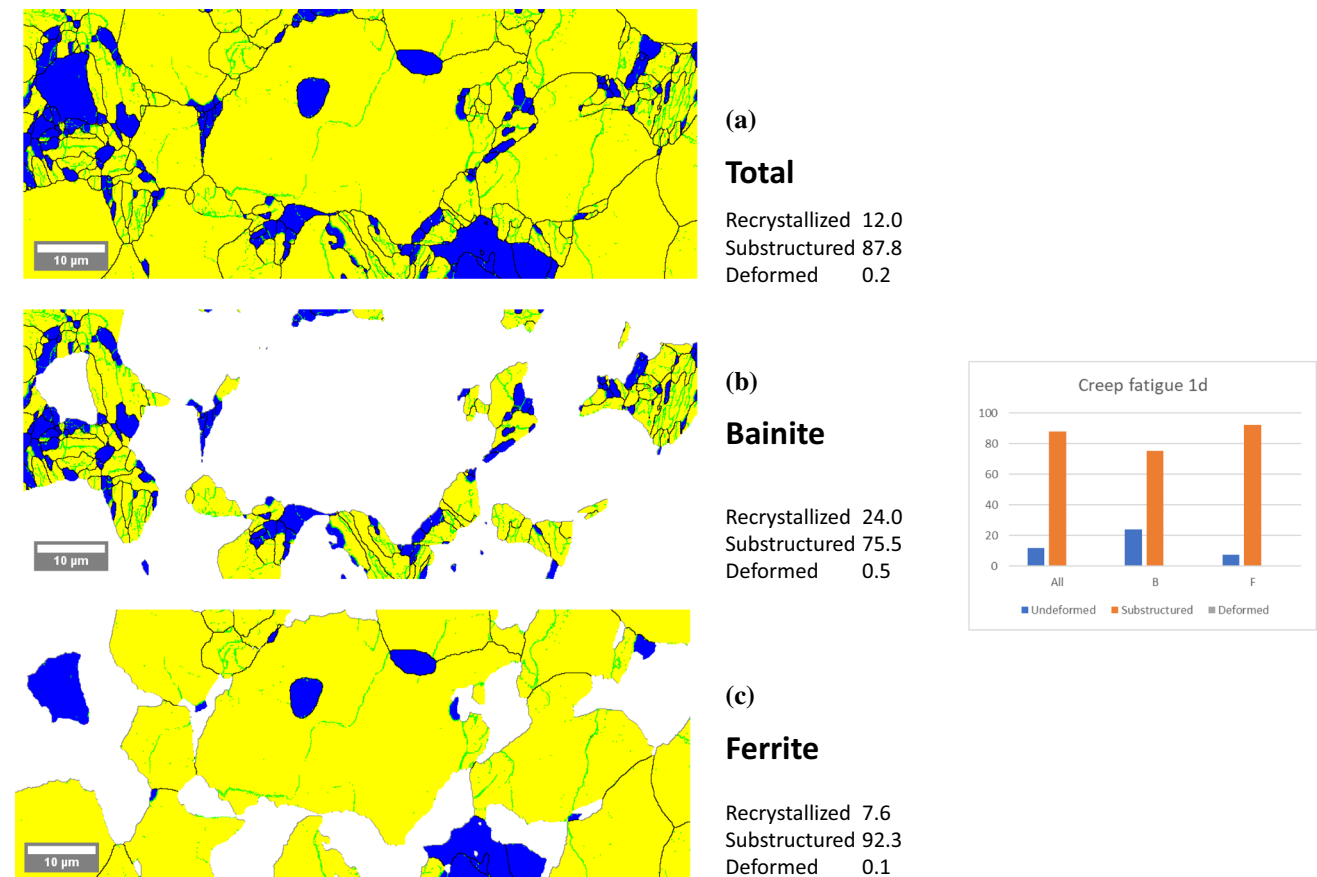
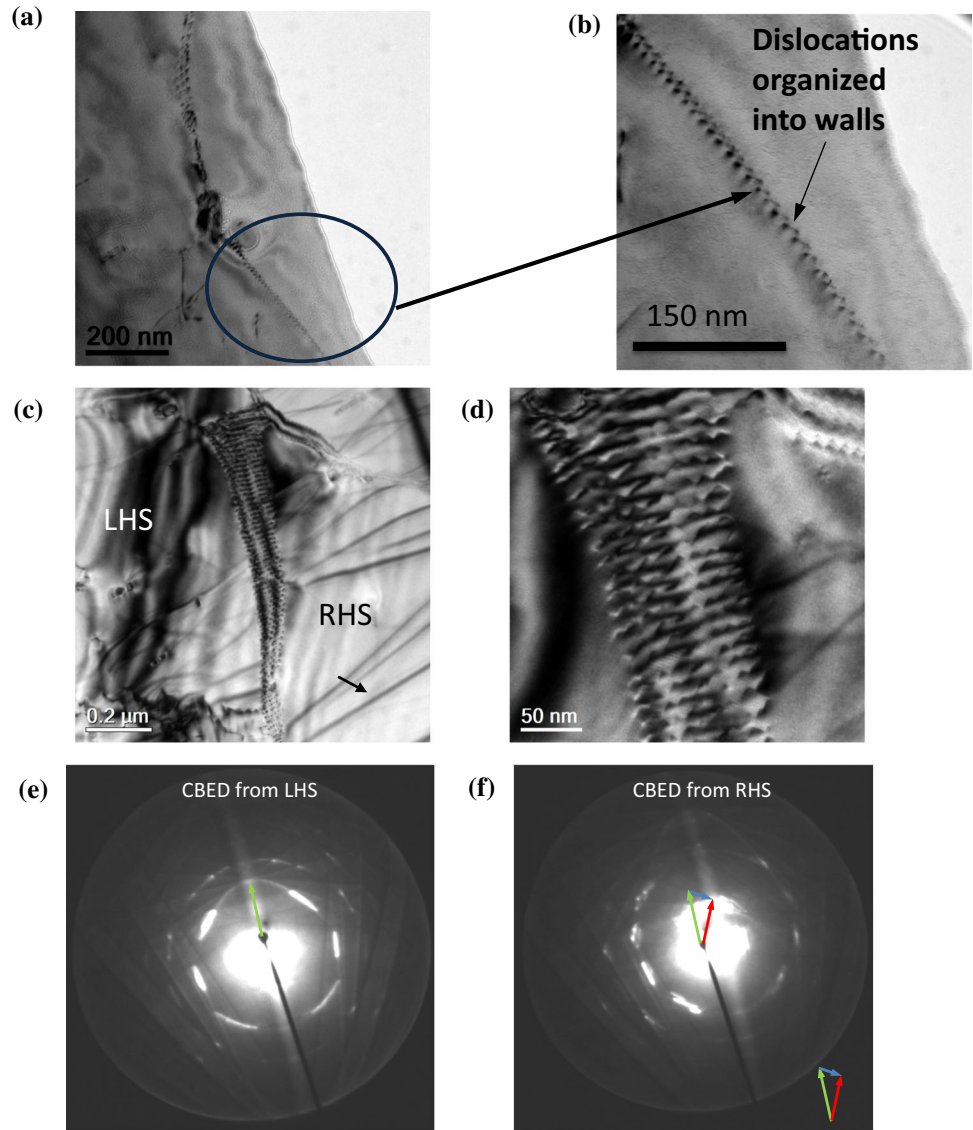


Figure 10 Creep-fatigue sample (550 °C)—recrystallized fraction—a total area, b bainite and c ferrite.

Figure 11 **a** Small-angle grain boundary in a clear ferrite grain and **b** detail of the same grain boundary showing individual dislocations, **c** and **d** subgrain boundary showing dislocations in an array with distance between dislocations ~ 16 nm; **e** CBED pattern from the left hand side and **f** CBED pattern from the right hand side of the grain boundary showing the rotation of the grain orientation by an angle corresponding to the blue arrow at the bottom right ($0.5\text{--}0.8^\circ$).



results in a state similar to a recovered structure in terms of a decrease in stored deformation or dislocation content. Thus, the dislocation density of the sample decreased during stress relaxation—this is consistent with other studies, which showed a decrease in dislocation density after stress relaxation in a Ni-based superalloy [37] and Cu alloys (C7025 and C7035) [38]. This result seems reasonable as the time at high temperature allows for the dislocations to be initially aligned in arrays to form subgrain boundaries, followed by subgrain growth until the interior of the prior grains becomes strain free. This process is thus similar to dynamic recovery, since there does not seem to be any significant migration of prior ferrite grain boundaries, as that would have

caused an change in the ferrite grain size, which is not observed here. It is also consistent with the fact that the SR tests were conducted at $550\text{ }^\circ\text{C}$ (823 K), which is above $0.4T_m$ ($T_m \sim 1700\text{ K}$), generally considered the threshold temperature for dynamic recovery [39]. This observation may explain the reason for decrease in creep life after SR tests, since the significant decrease in dislocation density due to these tests would reduce the yield strength (YS) of the material, which would, in turn, increase the creep rate and decrease the creep life. However, these changes would be visible only by EBSD or TEM, while being unobservable via optical microscopy, which may be the reason for these changes not being observed in the previous studies.

Table 3 Recrystallized (undeformed), substructured and deformed fractions for all samples (a) total scanned area, (b) ferrite regions and (c) bainite regions

	As-received	RT tensile	Hot tensile	Stress relaxation	Creep-fatigue
<i>Fraction of deformation state type in total scanned area (%)</i>					
Undeformed	37.5	2.5	7.5	32.5	12
Substructured	62.0	94.5	91.5	66.5	88
Deformed	0.5	3.0	1	1	0
<i>Fraction of deformation state type in ferrite (%)</i>					
Undeformed	61.5	1	6	59	7.5
Substructured	38.5	98.5	94	41	92.5
Deformed	0	0.5	0	0	0
<i>Fraction of deformation state type in bainite (%)</i>					
Undeformed	4	3.0	10.5	5	24
Substructured	94.5	92	88	93	75.5
Deformed	1.5	5	1.5	2	0.5

On the other hand, the creep-fatigue sample still shows subgrain boundaries, albeit at large distances in the ferrite grains. Thus, the size of the subgrains in the creep-fatigue sample is large (10–40 nm), but not large enough to encompass the entire ferrite grain. There is also more randomly distributed internal misorientation in the creep-fatigue sample compared to that in the stress-relaxed sample. The higher stored deformation in this case may be because of the shorter time that the creep-fatigue sample has experienced at high temperature (30 min after each extension step, instead of 168 h after each step in the stress relaxation case). In future work, more tensile and nanoindentation tests will be performed on stress-relaxed and creep-tested samples in order to determine the localized effect of the microstructural changes in the former, which leads to a degradation of the creep life in these samples.

Conclusions

Samples from Grade 22 (Fe–2.25%Cr–1%Mo) steel were subjected to a room temperature tensile test, a high-temperature tensile test at 550 °C, a stress relaxation test at 550 °C (23 cycles) and creep-fatigue test with a tension hold at 550 °C (128 cycles). The microstructure of the deformed samples, and that of the as-received sample, was examined using SEM, EBSD and TEM. Some of the salient observations that could be made from these samples are as follows:

1. The bainite phase constituent has much greater stored dislocation content in the form of SAGBs even in the as-received condition than the ferrite phase. This is found to be true also for all the other samples. This results in a higher local area misorientation in the bainite regions.
2. The RT tensile sample exhibited the greatest amount of deformation in the bainite regions, though the ferrite grains also experienced considerable plastic strain, as evident from the EBSD and TEM images. These dislocations in the ferrite have a tendency to form walls resulting in small subgrains (~100–200 nm). Some subgrain walls seem to originate from prior ferrite grain boundaries.
3. The HT tensile sample showed the clearing up of dislocations in both phases, but with considerably more cleaning up in the ferrite. Both phases showed > 87% “substructured” fraction.
4. The stress relaxation sample had the highest fraction of undeformed grains in the ferrite phase, where most of the grain area (~96%) is undeformed. Thus, in this material, the long periods of time at 550 °C under strain produced almost complete recovery and allowed subgrain growth.
5. The creep-fatigue sample has the largest fraction of substructured area, in the ferrite phase constituent, while having an appreciably large fraction of substructured area in the bainite phase as well. In this sample, the alternate straining and holding at high temperatures causes a relatively

Figure 12 **a** Fraction of recrystallized, substructured or deformed grains in total area (1d in the labels denotes that the subgrain boundary threshold was 1°), **b** fraction of recrystallized, substructured or deformed grains in ferrite (1d in the labels denotes that the subgrain boundary threshold was 1°) and **c** fraction of recrystallized, substructured or deformed grains in bainite (1d in the labels denotes that the subgrain boundary threshold was 1°).



high density of dislocations, which are organized into a subgrain structure with large subgrains. Here also, there seems to be some phenomenon akin to dynamic recovery in effect.

6. The large fraction of undeformed grains in the stress-relaxed samples might indicate the reason for decrease in creep life after SR tests, since it suggests that the yield strength would decrease leading to accelerated rupture in creep tests.

Data and code availability

The raw/processed data required to reproduce these findings cannot be shared at this time as the data also form part of an ongoing study.

There are no codes written specifically for this work. Any codes used in the processing of EBSD maps are part of the MTEX software used here [25].

Acknowledgements

The authors would like to acknowledge Mr. Tim Palmer and Mr. Kimbal Lu of NMDC, ANSTO, for their valuable support in sample preparation. The authors would like to acknowledge P. Dayal for his assistance in performing a few of the EBSD scans. This work has been funded by internal funding from Institute of Materials Engineering and Nuclear Fuel Cycle Research, ANSTO. The authors would also like to express their gratitude to the Nuclear Materials Development and Characterization platform (NMDC) for providing the characterization facilities essential for this work.

Declarations

Conflict of interest The authors do not have any known conflict of interest in the publication of this work.

Ethical approval Not applicable.

References

- [1] ASTM (1984) ASTM A335—Seamless ferritic alloy steel pipe for high temperature service, ASTM
- [2] Corwin WR, Burchell TD, Halsey WG, Hayner GO, Katoh Y, Klett JW, McGreevy TE, Nanstad RK, Ren W, Snead LL, Stoller RE, Wilson DF (2005) Updated generation IV reactors integrated materials program plan (Revision 2), In: Hadley PJ (ed) Oak Ridge National Laboratory
- [3] Dieter GE (1988) Mechanical metallurgy, Metric. McGraw-Hill, Singapore
- [4] Payten WM, Snowden KU, Dean DW (2013) Effects of prior stress relaxation on the prediction of creep life using time and strain based methods. *J Press Vessel Technol* 135(4):41201
- [5] Glover G, Sellars CM (1973) Recovery and recrystallization during high temperature deformation of α -iron. *Metall Trans* 4(3):765–775
- [6] Ouchi C, Okita T (1983) Dynamic recovery and static recrystallization of 1.8% al steel in hot deformation. *Trans Iron Steel Ins Jpn* 23(2):128–136
- [7] Storojeva L, Ponge D, Kaspar R, Raabe D (2004) Development of microstructure and texture of medium carbon steel during heavy warm deformation. *Acta Mater* 52(8):2209–2220
- [8] Liang S, Fazeli F, Zurob HS (2019) Effects of solutes and temperature on high-temperature deformation and subsequent recovery in hot-rolled low alloy steels. *Mater Sci Eng A* 765:138324
- [9] Humphries SR, Yeung WY, Callaghan MD (2011) The effect of stress relaxation loading cycles on the creep behaviour of 2.25Cr–1Mo pressure vessel steel. *Mater Sci Eng: A* 528(3):1216–1220
- [10] Fournier B, Sauzay M, Caës C, Noblecourt M, Mottot M, Allais L, Tournie I, Pineau A (2009) Creep-fatigue interactions in a 9 Pct cr-1 Pct Mo martensitic steel: part I. *Mech Test Res Metall Mater Trans A* 40(2):321–329
- [11] Alsmadi ZY, Abouelella H, Alomari AS, Murty KL (2022) Stress-controlled creep-fatigue of an advanced austenitic stainless steel at elevated temperatures. *Materials* 15(11):3984
- [12] Porter TD, Findley KO, Kaufman MJ, Wright RN (2019) Assessment of creep-fatigue behavior, deformation mechanisms, and microstructural evolution of alloy 709 under accelerated conditions. *Int J Fatigue* 124:205–216
- [13] Pohja R (2015) Creep-fatigue design of GEN IV high temperature reactor plants
- [14] IAEA (1996) Creep-fatigue damage rules for advanced fast reactor design, IAEA, Vienna
- [15] Bueno LO, Sobrinho JFR (2012) Correlation between creep and hot tensile behaviour for 2.25Cr-1Mo steel from 500 °C to 700 °C Part 1: an assessment according to usual relations involving stress, temperature, strain rate and rupture time revista. *Materia* 17(3):1098–1108

- [16] Ye W, Hu X, Song Y (2020) The relationship between creep and tensile properties of a nickel-based superalloy. *Mater Sci Eng A* 774:138847
- [17] Wei S, Kim J, Tasan CC (2022) In-situ investigation of plasticity in a Ti-Al-V-Fe ($\alpha+\beta$) alloy: slip mechanisms, strain localization, and partitioning. *Int J Plast* 148:103131
- [18] Rui S-S, Niu L-S, Shi H-J, Wei S, Tasan CC (2019) Diffraction-based misorientation mapping: a continuum mechanics description. *J Mech Phys Solids* 133:103709
- [19] Oh HS, Biggs K, Güvenç O, Ghassemi-Armaki H, Pottore N, Tasan CC (2021) In-situ investigation of strain partitioning and microstructural strain path development up to and beyond necking. *Acta Mater* 215:117023
- [20] Tu X, Shi X, Yan W, Li C, Shi Q, Shan Y, Yang K (2022) Tensile deformation behavior of ferrite-bainite dual-phase pipeline steel. *Mater Sci Eng A* 831:142230
- [21] Muránsky O, Zhu H, Lim S-L, Short K, Cairney J, Drew M (2020) On the evolution of mechanical properties and microstructure of ferritic-bainitic (FB) 2.25Cr-1Mo (Grade 22) steel during high-temperature creep. *Materialia* 9:100513
- [22] Fujita N, Ishikawa N, Roters F, Tasan CC, Raabe D (2018) Experimental–numerical study on strain and stress partitioning in bainitic steels with martensite–austenite constituents. *Int J Plast* 104:39–53
- [23] Humphries SR, Snowden KU, Yeung W (2010) The effect of repeated loadings on the stress relaxation properties of 2.25Cr–1Mo steel at 550 °C and the influence on the Feltham ‘a’ and ‘b’ parameters. *Mater Sci Eng A* 527(13):3240–3244
- [24] Humphries SR (2009) High temperature stress relaxation properties of ferritic pressure vessel steel, Faculty of Science, University of Technology Sydney, Sydney, 2009, pp 147
- [25] Bachmann F, Hielscher R, Schaeben H (2010) Texture analysis with MTEX—free and open source software toolbox. *Solid State Phenom* 160:63–68
- [26] Bacon R, Nutting J (1959) The tempering of 225Cr-1Mo steel after quenching and normalizing. *J Iron Steel Inst* 192(3):257–268
- [27] Hodgson DK, Dai T, Lippold JC (2015) Transformation and tempering behavior of the heat-affected zone of 2.25Cr-1Mo steel. *Weld J* 94:250-s–256-s
- [28] He SH, He BB, Zhu KY, Huang MX (2018) Evolution of dislocation density in bainitic steel: modeling and experiments. *Acta Mater* 149:46–56
- [29] Alsagabi S, Shrestha T, Charit I (2014) High temperature tensile deformation behavior of grade 92 steel. *J Nucl Mater* 453(1):151–157
- [30] Olmsted DL, Hector LG, Curtin WA, Clifton RJ (2005) Atomistic simulations of dislocation mobility in Al Ni and Al/Mg alloys. *Model Simul Mater Sci Eng* 13(3):371–388
- [31] Yu X-X, Wang C-Y (2009) The effect of alloying elements on the dislocation climbing velocity in Ni: a first-principles study. *Acta Mater* 57(19):5914–5920
- [32] McQueen HJ (1977) The production and utility of recovered dislocation substructures. *Metall Trans A* 8(6):807–824
- [33] Murty KL, Gollapudi S, Ramaswamy K, Mathew MD, Charit I (2013) Creep deformation of materials in light water reactors (LWRs), In: Murty KL (ed), *Materials ageing and degradation in light water reactors*, Woodhead Publishing 2013, pp 81–148
- [34] Carroll MC, Carroll LJ (2013) Developing dislocation subgrain structures and cyclic softening during high-temperature creep-fatigue of a nickel alloy. *Metall Mater Trans A Phys Metall Mater Sci* 44(8):3592–3607
- [35] Fournier B, Sauzay M, Barcelo F, Rauch E, Renault A, Cozzika T, Dupuy L, Pineau A (2009) Creep-fatigue interactions in a 9 Pct Cr-1 Pct Mo martensitic steel: Part II. *Microstruct Evolut*, *Metall Mater Trans A* 40(2):330–341
- [36] Reed-Hill RE, Abbaschian R (1994) *Elements of grain boundaries*, Physical metallurgy principles, PWS Publishing Company, Boston
- [37] Panwisawas C, D’Souza N, Collins DM, Bhowmik A (2017) The contrasting roles of creep and stress relaxation in the time-dependent deformation during in-situ cooling of a nickel-base single crystal superalloy. *Sci Rep* 7(1):11145
- [38] Xiao X, Xu H, Huang J, Wang J, Zhang J (2018) Stress relaxation properties and microscopic deformation structure in bending of the C7025 and C7035 alloy. *Crystals* 8(8):324
- [39] McQueen HJ (2001) Dynamic recovery and recrystallization. In: Buschow KHJ, Cahn RW, Flemings MC, Ilshner B, Kramer EJ, Mahajan S, Veysière P (eds) *Encyclopedia of materials: science and technology*. Elsevier, Oxford, pp 2375–2381

Publisher’s Note Springer Nature remains neutral with regard to jurisdictional claims in published maps and institutional affiliations.